Dielectrically driven convection in spherical gap geometry

Florian Zaussinger,[1] Peter Haun,[1] Matthias Neben,[1] Torsten Seelig,[1] Vadim Travnikov,[1] Christoph Egbers,[1] Harunori Yoshikawa,[2] and Innocent Mutabazi[3,*]

[1]*Department of Aerodynamics and Fluid Mechanics, Brandenburg University of Technology Cottbus-Senftenberg, Siemens-Halske-Ring 14, 03046 Cottbus, Germany*
[2]*Laboratoire J.-A. Dieudonné, UMR No. 7351, CNRS, Université Côte d'Azur, Parc Valrose, 06108 Nice Cedex 02, France*
[3]*Laboratoire Ondes et Milieux Complexes, UMR No. 6294, CNRS, Université du Havre, Normandie Université, 53 Rue de Prony, CS 80540, 76058 Le Havre Cedex, France*

Dielectric heating occurs in situations where an alternating electric field is applied on an insulating dielectric material. This effect can produce thermal convection in dielectric fluid through the thermoelectric coupling by the dielectrophoretic (DEP) force. The onset and the flow properties of the convection are investigated in a spherical gap geometry. The thermoelectrohydrodynamical equations often adopted in the modeling of the DEP-force-driven thermal convection are extended by an additional source term arising from the dielectric heating in the energy equation. Three-dimensional direct numerical simulations are performed, under microgravity conditions and without any imposed temperature gradient to highlight the effects of dielectric heating. In the conduction state, dielectric heating creates a parabolic temperature profile with a maximum in the interior of the spherical gap. In the convection state, the temperature distribution is more homogeneous with a lower maximum temperature. Numerical results are compared with interferograms from the GeoFlow II experiment performed on the International Space Station to validate the model. For the comparison, a numerical interferogram is applied to temperature fields obtained in the simulation. The onset of convection and basic spatial properties of the resulting internally heated convective zone are in good agreement with the experiment. The computed velocity fields reveal strong downdrafts which lead to recognizable fringe patterns in the interferograms.

I. INTRODUCTION

Heating materials by applying an electric field or by irradiating an electromagnetic field is a common practice in industry. The Ohmic effect and the dielectric loss are often used to generate heat energy inside materials. In the glass industry, electric glass furnaces are more frequently used because of the high efficiency, the smallness of apparatus, and the eco-friendliness [1]. Electric fields of 10–10^3 Hz in frequency are applied to glass materials (soda lime and sodium borate glasses) to melt by Ohmic heating. The heating generates temperature gradients to produce the convective motion in the melt. This convection is often modeled as thermal convection driven by the thermal Archimedean buoyancy force. The velocity and temperature fields of the melt are coupled with each other through an Ohmic heat generation term in the energy equation as well as in the thermal variations of fluid properties.

---

*Corresponding author: innocent.mutabazi@univ-lehavre.fr
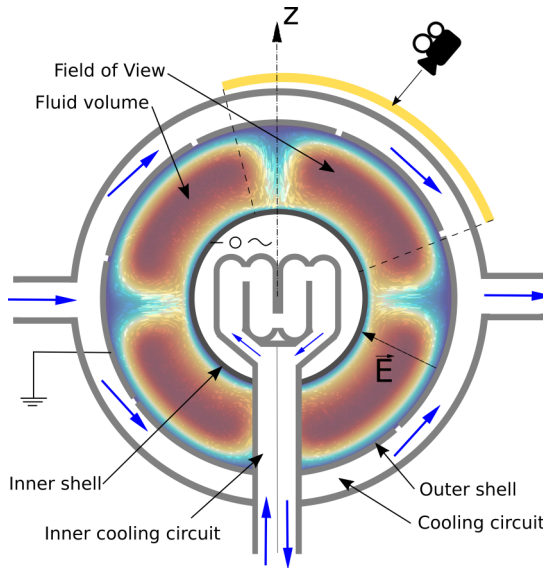
FIG. 1. Sketch of the convection experiment GeoFlow in a spherical geometry performed on the ISS. Red arrows depict the heating circuit and blue arrows the cooling circuit. Interferograms to visualize the temperature field are recorded in the region spanning from the north pole to the equator (yellow area). The depicted temperature field represents a typical convection zone induced by dielectric heating.

Dielectric heating plays an important role in many industrial and chemical applications where materials are thermally processed [2]. The most common application would be the domestically used microwave stove. While the physical process itself has been known since the late 19th century, it has become important with the work of von Hippel [3], which provides a database of properties of dielectric materials. This database was extended in the second half of the 20th century especially for many biological substances which are used in biochemistry and process engineering. The dielectric properties of important aqueous fluids were reviewed in Ref. [4] and more recently for biofuels (e.g., alcohols and their mixtures) in Ref. [5]. Dielectric heating is generated by a high-frequency electric field acting on a dielectric material. The field polarizes nonmotile charges in the material. There are two known types of polarization: (i) induced polarization due to the displacement of electrons inside atoms or molecules and (ii) orientation polarization due to permanent molecular dipoles aligned along the applied field. Heat energy is generated through the second type of polarization when the dipoles cannot respond to the temporal variation of an applied field with a phase delay.

The manifold influence of electric field on a fluid is a subject of thermoelectrohydrodynamics (TEHD). We refer to Refs. [6–9] for the theoretical background. Several laboratory experiments in the scope of TEHD have been reported in the literature. These experiments often use the dielectrophoretic (DEP) force to induce flows under microgravity conditions [e.g., on the International Space Station (ISS) or on parabolic flights]. The GeoFlow experiment (see Fig. 1) on the ISS represents such an experiment in the absence of earth's gravity field (see Ref. [10]). The main objective of the GeoFlow experiment was the investigation of thermal convection in the spherical gap, which is an analog of convection in planets or stars, under an imposed temperature gradient. However, the experimental setup also allows the study of dielectric heating and the influence of this process on thermal convection.

The investigation of convection induced by dielectric heating has been the object of many experimental and numerical works. Microwave-driven convective flows have been analyzed by different authors. Ayappa *et al.* [11] investigated water in a squared cavity and analyzed the uniformity of heating as a function of the power distribution. Detailed numerical simulations of

the coupled Maxwell and hydrodynamical equations have been performed by Zhang *et al.* [12] and Ratanadecho *et al.* [13]. More recently, Cherbański and Rudniak [14] investigated dielectrically driven convection in water. They showed with three-dimensional (3D) numerical simulations that dielectric heat-driven convection is not able to homogenize the temperature field, but produces temperature peaks. In the present paper, however, dielectric heat-driven convection is investigated in spherical gap geometry.

Natural convection in spherical gap geometries has been studied recently for the GeoFlow project, where centripetal gravity fields are simulated by the DEP force. We refer to Refs. [15,16] for details about the GeoFlow experiment. Theoretical and numerical investigations on the fundamental aspects of the DEP force-driven convection have been performed by Yoshikawa *et al.* [17], Fogaing *et al.* [18], Mutabazi *et al.* [19], Kang *et al.* [20], and Travnikov *et al.* [21] in different geometries. This paper extends these works by including the effects of dielectric heating and explains the occurrence of atypical convective patterns observed in the GeoFlow experiments.

The paper is organized as follows. The theoretical background of dielectric heating and extended TEHD equations are presented in Secs. I A and I B, respectively. The properties of the considered dielectric fluid and the experimental setup of GeoFlow are also given. Section II A is devoted to the basic conductive state of the system. The full set of TEHD equations is numerically treated in Sec. II B. A comparison between experimental interferograms and the numerical simulations is given in Sec. III. This paper ends with a detailed discussion and a summary.

A. Dielectric heating

Dielectric materials are electrical insulators with or without permanent molecular dipoles. In the case in which the material is placed in an electric field $\mathbf{E}$, permanent or induced dipoles are aligned along the electric field lines and can yield a macroscopic body force. In a dielectric fluid, the DEP force is induced by the application of an electric field. The force is proportional to the field squared and to the gradient of the permittivity ϵ:

$$\mathbf{F}_{\mathrm{DEP}} = -\tfrac{1}{2}\mathbf{E}^2 \boldsymbol{\nabla}\epsilon. \tag{1}$$

The permittivity of a dielectric fluid is given by $\epsilon = \epsilon_0 \epsilon_r$, where $\epsilon_0 = 8.854 \times 10^{-12}$ F/m is the vacuum permittivity and ϵ_r is the relative permittivity. The permittivity ϵ is in general a decreasing function of the fluid temperature, so a temperature gradient in a fluid leads to a DEP force. A high voltage and a strong thermal variation of ϵ are needed for a DEP force to be comparable to the gravitational force on earth. If a fluid in a spherical capacitor is subjected to a radial temperature gradient, the resulting DEP force is also radial and enables one to investigate thermal convection in a central force field.

Among other fluid properties, the permittivity has the most important influence on TEHD processes. The effects of fluid polarization in an alternating electric field can be treated conveniently in terms of the complex permittivity, which depends on the field frequency as well as on the fluid temperature:

$$\epsilon_r = \epsilon' - i\epsilon''. \tag{2}$$

The real part $\mathrm{Re}[\epsilon_r] = \epsilon'$ is called dielectric constant. The imaginary part $\mathrm{Im}[\epsilon_r] = \epsilon''$ represents the loss rate according to the conductance of the fluid. In an ac electric field $\mathbf{E}$ the electric displacement field is given by $\mathbf{D} = \epsilon_0 \mathbf{E} + \mathbf{P} = \epsilon_0 \epsilon_r \mathbf{E}$ for a linear isotropic dielectric, with $\mathbf{P} = (\epsilon_r - 1)\mathbf{E}$ the polarization. The polarization current density is $\mathbf{J}_{\mathrm{pol}} = \frac{\partial \mathbf{D}}{\partial t}$. Dielectric heating occurs in situations where the displacement $\mathbf{D}$ has a nonzero phase lag δ to the applied electric field $\mathbf{E}$. The tangent of δ, called the energy dissipation factor, is expressed as the ratio of the imaginary to real part of the permittivity

$$\tan \delta = \frac{\epsilon''}{\epsilon'}. \tag{3}$$

The power dissipation due to the dielectric loss per unit volume is

$$P = 2\pi f \epsilon_0 \epsilon' \tan \delta |\mathbf{E}|^2, \tag{4}$$

where f is the frequency of the electric field. For a given dielectric the energy loss depends mainly on the electric field strength and the frequency. For convenience, we define the rate of dielectric heating $S_{\mathrm{DH}} = P/\rho C_p$, with C_p the specific-heat capacity at constant pressure:

$$S_{\mathrm{DH}} = \frac{2\pi f \epsilon_0 \epsilon' \tan \delta |\mathbf{E}|^2}{\rho C_p}. \tag{5}$$

The rate of dielectric heating S_{DH} must be included in the law of energy conservation in order to simulate the influence of dielectric heating on a fluid.

B. Theoretical model

An electric field, applied on a dielectric fluid, induces three force densities

$$\mathbf{F} = \underbrace{\rho_V \mathbf{E}}_{\mathbf{F}_C} + \underbrace{\nabla \left[\frac{1}{2} \rho \left(\frac{\partial \epsilon}{\partial \rho} \right)_T \mathbf{E}^2 \right]}_{\mathbf{F}_{es}} + \mathbf{F}_{\mathrm{DEP}}. \tag{6}$$

The first term, called electrophoretic force, represents the Coulomb forces on free charges in the fluid. In an ac electric field with a frequency higher than all other characteristic frequencies involved in the flow dynamics, this force has no net effect on the fluid motion, since the force averaged over a period of field variation vanishes [17]. The second term is the electrostrictive force density $\mathbf{F}_{es}$. This force is a gradient force, so it has no effect on the motion of incompressible fluids with no mobile boundary. In the case of free surfaces or moving walls this force has to be taken into account. The dielectrophoretic force density $\mathbf{F}_{\mathrm{DEP}}$ [see Eq. (1)] remains as the prevailing force field. It is radially inward oriented and can be compared with a gravitational field. The TEHD equations governing the spatial and temporal evolution of the velocity field $\mathbf{u}$, the electric field $\mathbf{E}$, and the temperature field T are [19]

$$\nabla \cdot \mathbf{u} = 0, \tag{7}$$

$$\frac{\partial \mathbf{u}}{\partial t} + (\mathbf{u} \cdot \nabla)\mathbf{u} = -\nabla \Pi + \nabla \cdot \bar{\bar{\tau}} + \rho_0^{-1} \mathbf{F}_{\mathrm{DEP}}, \tag{8}$$

$$\frac{\partial T}{\partial t} + (\mathbf{u} \cdot \nabla)T = \kappa_T \nabla^2 T + S_{\mathrm{DH}}, \tag{9}$$

$$\nabla \cdot \mathbf{E} = 0, \tag{10}$$

where we have adopted the electrohydrodynamic Boussinesq approximation [22]. Equation (7) is the mass conservation for incompressible flows. Equation (8) is the Navier-Stokes equation, with $\bar{\bar{\tau}}$ being the viscous stress tensor. The electrostrictive force $\mathbf{F}_{es}$ is lumped with the pressure [19], resulting in an effective pressure term $\Pi = \frac{1}{\rho_0}[P - \frac{1}{2}\rho(\frac{\partial \epsilon}{\partial \rho})_T \cdot |\mathbf{E}|^2]$. Equation (9) is the energy equation, which describes the evolution of temperature, with κ_T the thermal diffusion coefficient. The rate of dielectric heating S_{sh} is included in this equation for examining the effects of dielectric heating on the flow field. Equation (10) is the Gauss equation. We have assumed that the free charge density of the dielectric is negligible. We have also neglected the thermal variation of the permittivity in the Gauss equation. In a geometry with a large curvature, as considered in the present work, the spatial variation of the electric field arises primarily from the geometry curvature.

The governing equations (7)–(10) are completed by the equation of state for the permittivity ϵ. For a small temperature deviation from a reference value T_0, it is given by

$$\epsilon = \epsilon_{\mathrm{ref}}[1 - \alpha_E(T - T_0)], \tag{11}$$

where α_E is the dielectric expansion factor and ϵ_{ref} is the permittivity at $T = T_0$ [15,17,19]. We apply Eqs. (7)–(11) to a dielectric fluid in the gap of two concentric electrodes. Each electrode is maintained at a constant temperature and a high-frequency ac electric voltage is imposed over the gap. The temperature field in the conduction state is given [19] by

$$T_b(r) = T_2 + \frac{\eta(T_1 - T_2)}{1 - \eta}\left(\frac{R_2}{r} - 1\right), \tag{12}$$

where (R_1, T_1) and (R_2, T_2) are the radius and the temperature of the inner and outer electrodes, respectively. The radius ratio is defined by $\eta = R_1/R_2$. In an electric voltage of a frequency higher than the reciprocal of the viscous timescale, only the time-averaged component of the DEP force can affect the fluid motion. This component can be calculated from the effective electric field, which is given in the conduction state [19] by

$$\mathbf{E}_b(r) = -\frac{\eta V_{\text{rms}}}{R_2 - R_1}\frac{B}{\ln(1 - B)}\left(\frac{R_2}{r}\right)^2\left[1 - B\frac{T_b(r)}{\Delta T}\right]^{-1}\mathbf{e}_r, \tag{13}$$

where $B = \alpha_E \Delta(T_1 - T_2)$ is the thermoelectric parameter, $V_{\text{rms}} = V_0/\sqrt{2}$ is the effective voltage, and $\mathbf{e}_r$ is the radial unit vector. In the present work, we will focus on the case where no temperature gradient is imposed, i.e., $B \to 0$, and in the electrode geometry of $\eta = 0.5$ ($R_2 = 2R_1$). The effective electric field is then given by

$$\mathbf{E} = \frac{R_1 R_2}{R_2 - R_1}\frac{V_0}{\sqrt{2}}\frac{1}{r^2}\mathbf{e}_r. \tag{14}$$

Neither temperature nor the velocity field influence the electric field (14) in this model. In the case of strong temperature-dependent permittivity or low curvatures $\eta > 0.7$ the coupling between the momentum, energy, and Gauss equation has to be taken into account. The effects of the DEP force are comparable to those of the thermal Archimedean buoyancy force in earth's gravity field. The wording *electric gravity* has been established for the effective acceleration of the dielectric origin,

$$\mathbf{g}_e = \frac{\alpha_E}{\rho_0\alpha_T}\nabla\left(\frac{\epsilon_0\epsilon'\mathbf{E}^2}{2}\right). \tag{15}$$

Further, this motivates the electric Rayleigh number as given in [19],

$$\text{Ra} = \frac{\alpha_T \Delta T \mathbf{g}_e (R_2 - R_1)^3}{\nu\kappa_T}, \tag{16}$$

with ν the kinematic viscosity and ΔT a representative value of the temperature variation inside the fluid.

The governing TEHD equations are analyzed in two ways. First, we focus on the conductive base state for a given electric field $\mathbf{E}$ in the spherical capacitor. This gives a rough estimate about timescales and the spatial temperature profiles. Second, the equations are solved numerically in three-dimensional space. Both issues require detailed information about the experimental setup, the geometry, the resulting parameter space, and the fluid properties. These properties are presented in the following.

C. Fluid properties and flow conditions

The present investigation is performed for the flow conditions realized in the GeoFlow experiments, which can provide results for comparison. The GeoFlow experiments were performed in the Fluid Science Laboratory of the Columbus module on the ISS between 2008 and 2017. Two missions have been accomplished. The first mission GeoFlow I (2008) was performed using the isoviscous silicon oil M5, which is a nonpolar liquid. Hence, the fluid is not susceptible for dielectric heating. The second mission GeoFlow II (2011–2017) examined the effects of the

TABLE I. Properties of 1-Nonanol for two reference temperatures at a frequency of 1.0650×10^4 Hz.

Property	$T_0 = 293.0$ K	$T_0 = 303.5$ K
Energy dissipation factor $\tan \delta$	6.12×10^{-2}	7.45×10^{-2}
Relative permittivity ϵ'	9.3	8.44
Density ρ (kg/m^3)	8.29×10^2	8.22×10^2
Specific-heat capacity C_p (J/K)	2.47×10^3	2.47×10^3
Thermal diffusivity κ_T (m^2/s)	7.94×10^{-8}	7.76×10^{-8}

temperature-dependent viscosity on convection with adopting 1-Nonanol as the working fluid. The molecules of the 1-Nonanol have a strong dipole moment due to a hydroxyl group. This makes the fluid susceptible to dielectric heating. All relevant fluid properties are listed in Table I. They are based on measurements of the electrical properties provided by Airbus Defense and Space (formally EADS Astrium). The experiment consists of two concentric shells, which can rotate around a central axis. The inner and outer spherical electrodes have radii of $R_1 = 0.0135$ m and $R_2 = 0.027$ m (radius ratio is $\eta = 0.5$), respectively (see Fig. 1). Electrodes are maintained at constant temperatures. The temperature at the outer shell was considered as the reference value T_0, adjusted to either 293.0 K or 303.5 K. Electric voltage is limited by a maximum value $V_0 = 6500$ V. The peak value of the electric gravity is reached at the inner sphere, where $g_e \approx 13$ m/s^2. The lowest value is measured at the outer sphere where $g_e \approx 0.3$ m/s^2. The Rayleigh number is varied over five magnitudes, $5.6 \times 10^2 < \text{Ra} < 1.43 \times 10^7$.

For a given fluid, control parameters are the temperature difference $T_1 - T_2$ between the electrodes, the applied voltage V_0, and the rotation rate Ω. In the present investigation, we consider only initially isothermal experimental runs ($T_1 = T_2$) with no rotation of the electrodes ($\Omega = 0$). In the GeoFlow II experiment, the maximum electric field strength varies between 1.9×10^5 V/m for
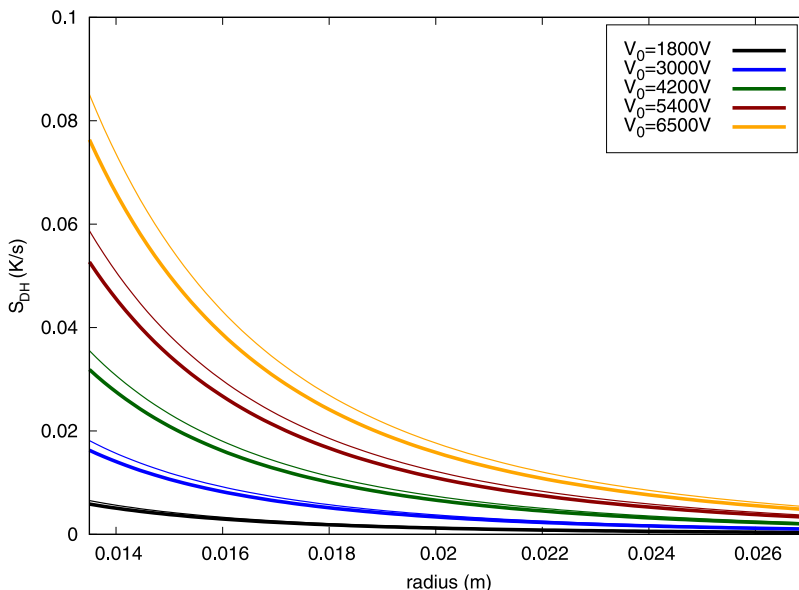
FIG. 2. Radial profiles of the dielectric heating rate S_{DH} [Eq. (5)] for 1-Nonanol at different values of the electric voltage. The fluid properties are listed in Table I. Thin lines correspond to $T_0 = 293.0$ K, and thick lines to $T_0 = 303.5$ K. The highest heating rate is found for $V_0 = 6500$ V at the inner shell.
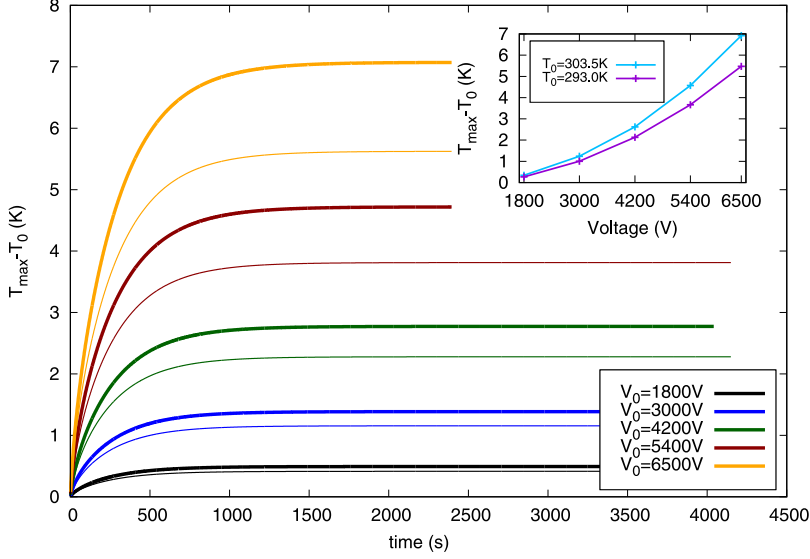
FIG. 3. Temporal evolution of the maximum temperature in the conduction state for $T_0 = 293.0$ K(thin lines) and for $T_0 = 303.5$ K(thick lines). The inset depicts the saturated maximum temperature as a function of the voltage for both reference temperatures.

$V_0 = 1800$ V and 6.9×10^5 V/m for $V_0 = 6500$ V. Figure 2 depicts S_{DH}, calculated from Eqs. (5) and (13), for various voltages and reference temperatures examined in the experiment. A maximum of 0.085 K/s is obtained for $V_0 = 6500$ V at the inner electrode. The resulting temperature profile is obtained by solving Eq. (9) under the boundary condition of constant temperatures at the electrodes.

II. NUMERICAL SIMULATIONS

A. Conductive state

In the conduction state ($\mathbf{u} = \mathbf{0}$), the energy equation (9) reads

$$\frac{\partial T}{\partial t} = \kappa_T \left(\frac{\partial^2 T}{\partial r^2} + \frac{2}{r} \frac{\partial T}{\partial r} \right) + S_{\mathrm{DH}}(\epsilon'(T), V_0, r). \qquad (17)$$

The calculation of the source term $S_{\mathrm{DH}}(\epsilon'(T), r)$ is based on the thermal variation of the permittivity and the energy dissipation factor measured in the laboratory (Sec. I C),

$$\epsilon'(T) = -0.511\,03T + 97.467 + 7.1429 \times 10^{-4} T^2, \qquad (18)$$

$$\tan \delta(T) = -4.606 \times 10^{-1} T + 47.37 - 1.594 \times 10^{-6} T^3 + 1.488 \times 10^{-3} T^2, \qquad (19)$$

where the temperature is given in kelvins. Equation (17) has been solved by a simple, explicit finite-difference scheme. To guarantee a stable solution a Courant-Friedrichs-Lewy number of 0.25 was chosen for 100 cells. Both reference temperatures $T_0 = 293.0$ and 303.5 K, and five values of V_0 have been tested. The boundaries are kept at the reference temperature $T_1 = T_2 = T_0$. In contrast to the heating rate plotted in Fig. 2, the maximum temperature is not obtained at the inner shell. Within the first thermal timescale $\tau = (R_2 - R_1)^2 / \kappa_T = 2603$ the temperature profile becomes stationary. This is shown for both reference temperatures in Fig. 3, where the difference of the maximum temperature $T_{\max}$ and the reference temperatures is plotted over the thermal timescale.
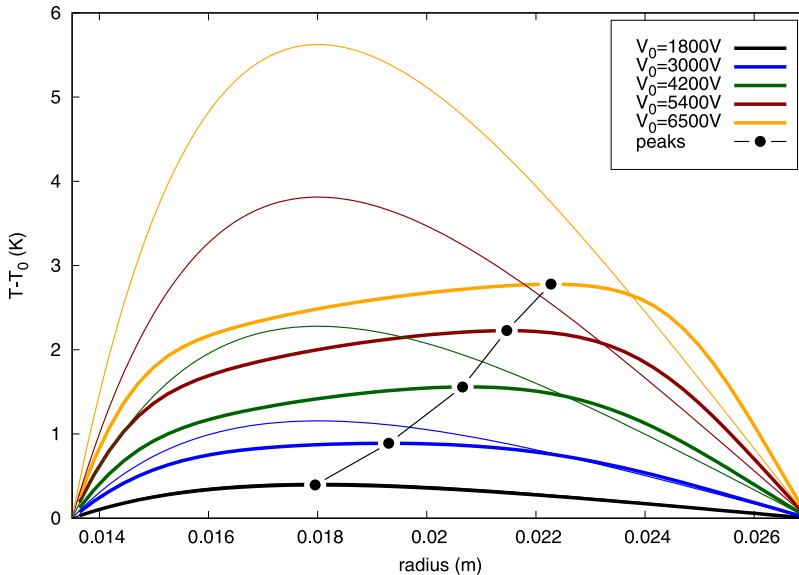
FIG. 4. Radial temperature profiles in the spherical gap with dielectric heating. The conductive solution obtained from Eq. (17) (thin lines) and latitude- and longitude-averaged temperature profiles computed from the 3D simulations (thick lines) are shown for $T_0 = 293.0$ K. The black long-dashed line connects temperature maxima. The profiles for $V_0 = 1800$ V coincide.

The conductive case reveals a paraboliclike temperature profile where the minima are located at the boundaries and the maxima are found in the interior (see Figs. 4 and 5). In all 1D solutions the position of T_{max} is found at $r_{max} = 0.0179$ m, or $r_{max}/R_2 = 0.665$. The slope dT_{max}/dV_0 increases with the reference temperature (Fig. 3, inset).

B. Three-dimensional simulations

The governing equations (7)–(9), incorporating the electric field given by Eq. (14), are solved numerically with the finite-volume method using the open source software suite OpenFOAM® [23]. A cubed sphere grid is used for all simulations. No-slip boundary conditions are imposed on the velocity field at the electrode surfaces. The thermal boundary conditions are of Dirichlet type, i.e., constant temperatures. The code solves dimensional equations in three dimensions with the PISO algorithm. Time integration is performed with an implicit Crank-Nicolson method. The spatial derivatives are approximated in second order. Subgrid scales are modeled using a one-equation ansatz for the turbulent kinetic energy. The accuracy of the results is given with a maximum residual of 10^{-6}. Several tests have been performed to guarantee converged solutions. A detailed grid study showed that the total energy converges towards a fixed value for 4×10^6 cells. This resolution also resolves the thermal boundary layers with at least five cells. In addition, the latitude- and longitude-averaged temperature profiles are analyzed. These profiles (see Fig. 4) do not change for more than 4×10^6 cells.

The GeoFlow experiment visualizes results as interferograms. They are obtained by a Wollaston shearing interferometry which measures first derivatives of the fluid refractive index. These derivatives are identified as temperature derivates through nearly identical slopes. Advanced numerical postprocessing techniques are necessary to reconstruct the underlying temperature and velocity field. An approved approach is the backward reconstruction, where numerical interferograms are compared with experimental ones. In the case in which the interferograms match in predefined characteristics (e.g., size, number, and speed of convective plumes), the internal field in the experiment is assumed to be identical to the numerical simulations. To compare simulations and the
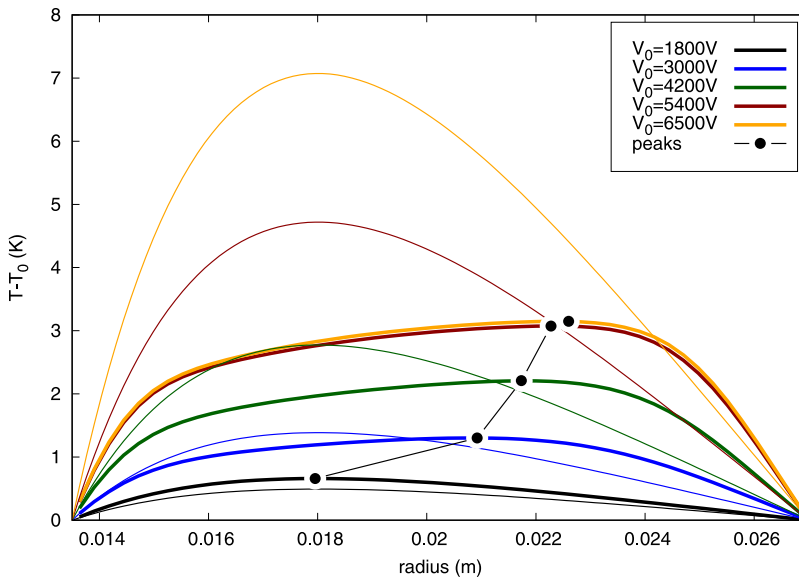
FIG. 5. Radial temperature profiles in the spherical gap with dielectric heating. The conductive solution obtained from Eq. (17) (thin lines) and latitude- and longitude-averaged temperature profiles computed from the 3D simulations (thick lines) are shown for $T_0 = 303.5$ K. The black long-dashed line connects temperature maxima.

experimental images, numerical interferograms $I(x, y)$ are calculated according to the algorithm presented in Ref. [24]. We define the numerical interferometry function

$$I(x, y) = -\cos\left(a_{\text{fringe}}\frac{\partial T_{\text{mean}}}{\partial \mathbf{s}} + bx + cy\right), \tag{20}$$

where a_{fringe} is a control parameter for the density of fringes, T_{mean} is the radially averaged temperature, and $\mathbf{s}$ is the direction of polarization. The interferometric base pattern is implemented by a linear extension of the mean-temperature derivative function with constants b and c. By changing these values, the amount and direction of the base pattern are controlled. For our simulations we use $a_{\text{fringe}} = 0.05$, $b = -200$, and $c = 600$. The numerical interferograms are evaluated in the same area as the experimental interferograms. This is shown in Fig. 6, where the patch of the numerical interferogram is spanned over the outer shell of the experiment. The interferograms show two typical patterns: first, double-ring structures which originate from thermal plumes, and second, parallel lines of fringes which are caused by sheetlike structures. A detailed analysis of these structures is presented in Ref. [24].

All simulations follow the exact timeline of the experiment as shown in Fig. 7. A high voltage and a uniform temperature field at a predefined reference temperature are applied for at least 61 min before the interferograms are recorded. We have also taken into account the initial temperature distribution in the fluid, which is estimated from the ambient temperature of the ISS. Our numerical study covers ten parameter sets, including five voltages $V_0 = 1800$, 3000, 4200, 5400, and 6500 V as well as two reference temperatures $T_0 = 293.0$ and 303.5 K.

C. Thermal stratification and heat transfer

The conductive solutions show parabolic profiles at the temperature where the maxima are found in the interior of the gap and the minima are located at the boundaries. This stratification is also found in the 3D simulations. The results of the 1D and 3D calculations are compared in Fig. 4 for
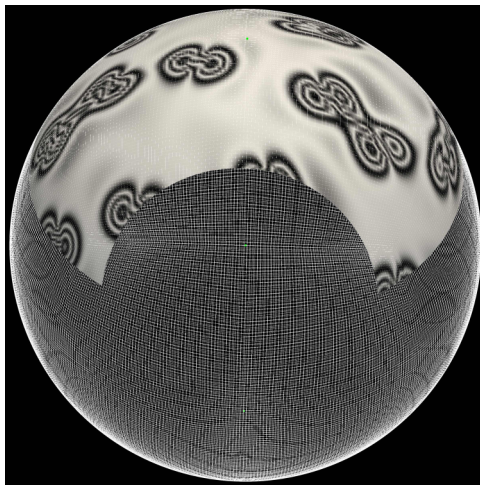
FIG. 6. Area of the numerical interferogram congruent with the experimental interferogram of GeoFlow for $V_0 = 6500$ V and $T_0 = 293.0$ K.

$T_0 = 293.0$ K and in Fig. 5 for $T_0 = 303.5$ K. Thin lines are stationary solutions for the conductive case and thick lines are latitude- and longitude-averaged temperature profiles of 3D simulations. The long-dashed black line connects peak values of the temperature. The location of the temperature peak moves towards the outer shell for increasing voltages, contrary to the conductive case, where the location of the peak is always found at $r_{max}/R_2 = 0.665$ for both reference temperatures. For $V_0 = 1800$ V and $T_0 = 293.0$ K the 1D and the 3D profiles coincide (black lines). It follows that this case is also conductive in three dimensions, even though the profile shows a negative temperature gradient in the outer half of the gap. The case of $V_0 = 1800$ V and $T_0 = 303.5$ K differs. Here the profile from the 3D simulation is always above the 1D conductive solution. The onset of convection will be found within 1800 V $< V_0 <$ 3200 V, where an octahedral convective structure is observed for $V_0 = 3000$ V in the numerical simulations.

The heat transfer is described in terms of the Nusselt number

$$\text{Nu} = \frac{F_{tot}}{F_{cond}}, \tag{21}$$

where F_{tot} is the total heat flux, incorporating the convective and the conductive flux. To calculate the total heat flux at the electrodes the temperature field is averaged in the latitude and in the longitude and then differentiated in the radial direction. The conductive flux F_{cond} is given by the solutions of the extended heat (17). Figure 8 shows the Nusselt number calculated at the inner (subscript i) and the outer (subscript o) shells for both reference temperatures and as a function of the voltage.
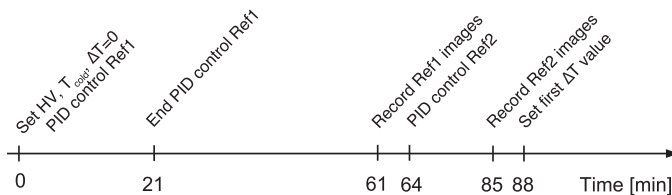
FIG. 7. Time line of experimental runs of GeoFlow II. Two series of reference images (Ref1 and Ref2) are recorded with $\Delta T = 0$ and high voltage V_0. Ref1 is recorded after 61 min and Ref2 after 85 min. Both reference series are used to measure the influence of dielectric heating on the conductive state.
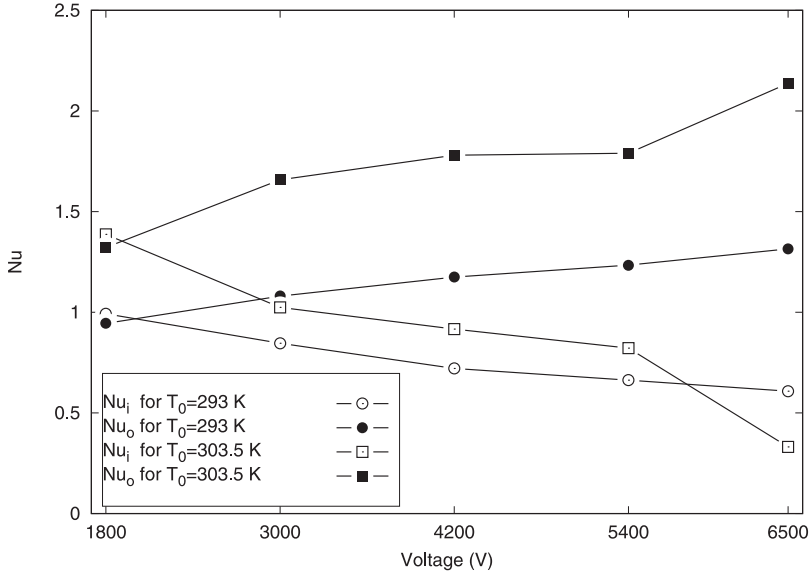
FIG. 8. Nusselt number as a function of the voltage. Closed and open symbols show the Nusselt numbers measured at the outer shell Nu_o and the inner shell Nu_i, respectively.

The value of Nu_i is always decreasing with the voltage, while Nu_o increases with the voltage. The slopes of both graphs are opposite, resulting in a nearly constant averaged arithmetic mean value of Nu (not shown). The Nusselt numbers differ between the reference temperatures. Their values for $T_0 = 303.5$ K are always higher than those for $T_0 = 293.0$ K. Even the assumed conductive case of $V_0 = 1800$ V reveals a Nusselt number of Nu = 1.5. In contrast to the classical Rayleigh-Bénard (RB) convection, the Nusselt numbers at the inner shell are also less than unity. This comes from the fact that the convective flux becomes negative in the inner part of the spherical gap. This is a distinctive feature of the TEHD convection under dielectric heating. In the RB convection, the convective flux is always greater than (convection state, Nu > 1) or equal to (conduction state, Nu = 1) the conductive flux. In the TEHD convection under dielectric heating, therefore, the onset of convection cannot be detected anymore with the criterion Nu > 1.

A strong influence of the convective flow on the temperature profile is observed for $V_0 > 3000$ V. The maxima are "eroded" by the velocity field towards the outer shell, where the convective flux is positive and greater than the conductive flux. This explains the differences between the inner and the outer Nusselt numbers. It is observed that convective cells penetrate the stably stratified bottom region, which results in convection cells extending over the whole gap.

III. COMPARISON WITH EXPERIMENT

A. Temperature field

A comparison of experimental interferograms and the numerical results for different values of the voltage is shown in Figs. 9 and 10. The first row depicts the experimental interferograms and the second row the numerical interferograms. The third and fourth rows show the temperature and velocity fields in a meridian plane.

In all experimental interferograms the base pattern of the Wollaston shearing interferometry unit is visible as stripes. This pattern is produced because of the manufacturing tolerance of the shells. The first column ($V_0 = 1800$ V) does not exhibit any convective structures for both reference temperatures. Three explanations are possible: First, the interferometry is not sensitive enough to

	$V_0 = 1800\,\mathrm{V}$	$V_0 = 3000\,\mathrm{V}$	$V_0 = 4200\,\mathrm{V}$	$V_0 = 5400\,\mathrm{V}$	$V_0 = 6500\,\mathrm{V}$
Experimental interferogram $\Delta T = 0\,\mathrm{K}$ $T_0 = 293.0\,\mathrm{K}$	(a)	(b)	(c)	(d)	(e)
Numerical simulation $\Delta T = 0\,\mathrm{K}$ $T_0 = 293.0\,\mathrm{K}$	(f)	(g)	(h)	(i)	(j)
temperature slice	(k)	(l)	(m)	(n)	(o)
radial velocity	(p)	(q)	(r)	(s)	(t)
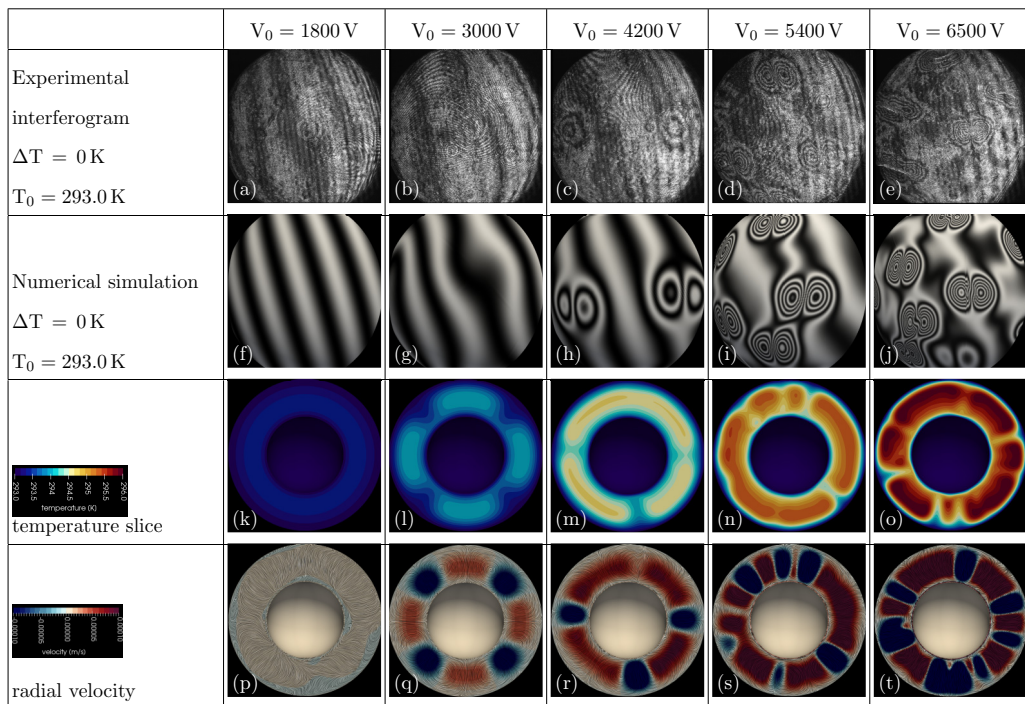
FIG. 9. (a)–(e) Experimental interferograms of the GeoFlow II experiment for $T_0 = 293.0$ K and $\Delta T = 0$. (f)–(j) Numerically calculated interferograms based on 3D simulations. Both rows show interferograms recorded after $t = 2603$ s. Dielectric heating is visible for $V_0 \geqslant 4200$ V as thermal plumes which exhibit characteristic double-ring structures. Conductive cases (a) and (b) show only the base fringe pattern. (k)–(o) Temperature distribution in a vertical slice. (p)–(t) Streamlines colored by the radial velocity field. Blue regions are downdrafts and red regions are updrafts.

resolve weak temperature gradients; second, the experiment timescale is too short for convective flow to develop; third, the conduction state is stable at this voltage.

Convective plumes at $V_0 = 3000$ V show weak gradients and are hard to identify in the interferograms. They are indicated by sightly distorted fringes. On the other hand, the plumes are visible in the numerical simulations as regular octahedral structures. These structures have also been observed by Zaussinger *et al.* [24] and Feudel *et al.* [25]. For $V_0 \geqslant 4200$ V convective plumes are visible as double rings in the experiment and in the numerical simulations. The number of rings is positively correlated to the voltage and to the reference temperature. Due to the increased acceleration at higher voltages, the thermal gradients steepen and the frequency of fringes in double-ring packages increases. This holds for both reference temperatures. It may be worth mentioning that sheetlike structures are never observed under the isothermal condition $T_1 = T_2$. The size of convective plumes decreases with increasing voltage. See, for instance, the results for $T_0 = 303.5$ K and $V_0 = 4200$–6500 V. The observed behavior of plumes is in good agreement with RB convection, where convective plumes are described as thermal boundary layers separated from walls. The boundary layers get thinner with increasing Rayleigh number. The thermal gradients then become steeper. In addition, the size of the plumes depends on the reference temperature. Plumes are larger for $T_0 = 293.0$ K. By comparing the temperature field [Figs. 9(o) and 10(o)] or the radial velocity field [Figs. 9(t) and 10(t)] observed at different temperatures, one finds steeper plumes at the higher temperature $T_0 = 303.5$ K.

The selected images are representative of the amount of convective cells found. They are obtained by manually counting. For both reference temperatures we find a positive correlation between

	$V_0 = 1800\,\mathrm{V}$	$V_0 = 3000\,\mathrm{V}$	$V_0 = 4200\,\mathrm{V}$	$V_0 = 5400\,\mathrm{V}$	$V_0 = 6500\,\mathrm{V}$
Experimental interferogram $\Delta T = 0\,\mathrm{K}$ $T_0 = 303.5\,\mathrm{K}$	(a)	(b)	(c)	(d)	(e)
Numerical simulation $\Delta T = 0\,\mathrm{K}$ $T_0 = 303.5\,\mathrm{K}$	(f)	(g)	(h)	(i)	(j)
temperature slice	(k)	(l)	(m)	(n)	(o)
radial velocity	(p)	(q)	(r)	(s)	(t)
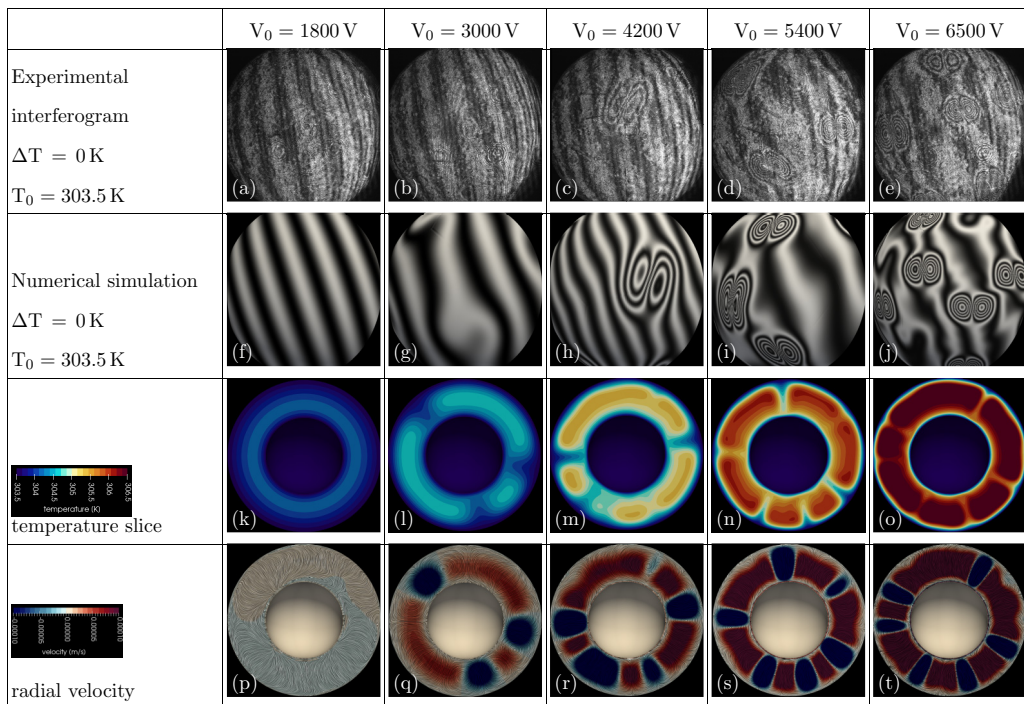
FIG. 10. (a)–(e) Experimental interferograms of the GeoFlow II experiment for $T_0 = 303.5$ K and $\Delta T = 0$. (f)–(j) Numerically calculated interferograms based on 3D simulations. Both rows show interferograms recorded after $t = 2603$ s. Dielectric heating is visible for $V_0 \geqslant 4200$ V as thermal plumes which exhibit characteristic double-ring structures. Conductive cases (a) and (b) show only the base fringe pattern. (k)–(o) Temperature distribution in a vertical slice. (p)–(t) Streamlines colored by the radial velocity field. Blue regions are downdrafts and red regions are updrafts.

plumes and voltage. Up to 20 plumes are found per hemisphere in the case of $V_0 = 6500$ V. In the statistical mean we find 38% more convection cells in the numerical simulations than in the experiment. This aberration will be discussed in Sec. IV. The numerical simulations reveal that the convective plumes emerge irregularly in the spherical gap. They are not stationary, but are moving and relocated within 10–20 min over the distance of the interferogram. As the experimental interferogram measurement lasts only 3 min, it is not possible to estimate the velocities of plumes for comparisons with the numerical results.

B. Size of double-ring structures

The inner structure of double rings depends on the temperature gradients inside the convective plume. In addition, the temperature distribution in the midgap spherical surface looks Gaussian around a plume. As the interferometry delivers narrower stripes at higher gradients, the two centers of the double rings represent inflection points. These points are located at $\mu \pm \sigma$, where μ is the bisection point of the double-ring centers. The temperature takes its local maximum or minimum there. The length between two centers ($l_c = 2\sigma$) gives a quantitative value for the width of a convective plume which is used to calibrate numerical interferograms. Additionally, l_c depends on the velocity field and the thermal distribution due to dielectric heating. We calculate the mean value of all visible plumes to calibrate the numerical interferograms. The variation of this mean value is within 10%, which indicates that the lateral elongation of the plumes is nearly identical. We find the
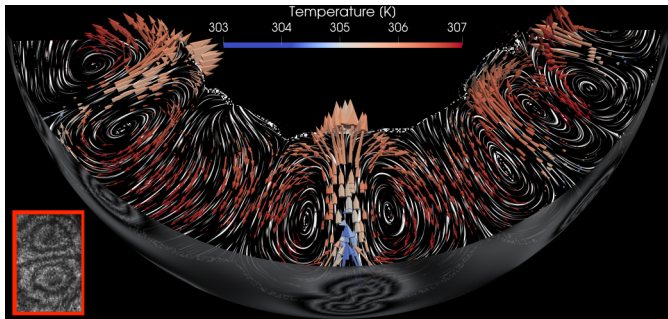
FIG. 11. Velocity vectors and associated streamlines along a convective downdraft. The double-eye pattern occurs from a downward stream, where cold material is transported towards the inner shell. The red box shows an experimental interferogram.

same result in the numerical simulations by analyzing the temperature field in the meridian surface. Double-ring structures at $T_0 = 303.5$ K are generally wider than for $T_0 = 293.0$ K.

C. Velocity field

Interferograms do not deliver direct quantitative information about the velocity field. By careful confrontation of the experimental and numerical interferograms, however, it is possible to deduce some properties of the flow velocities. The simulations show that the convective flow is enhanced by the increase of the applied electric voltage, as expected from the analogy to the classical RB convection. Furthermore, the simulations show peak velocities at the locations of downdrafts, underneath double-ring structures. The mean velocity in updraft regions is about halved. The last rows in Figs. 9 and 10 show this behavior. Blue regions, where the radial velocity points inward, coincide with steep thermal plumes. This observation differs from earlier publications about GeoFlow II, where updrafts were predicted in the same situations. We will discuss this point in Sec. IV. The velocity field in such a downdraft region is shown in Fig. 11 in more detail, where streamlines are superimposed on the velocity vectors. The colors of the vectors indicate the temperature values. One can see that the velocities are larger in the inner half layer than in the outer half layer. This would be a consequence of (i) an increased radial acceleration due to the dielectrophoretic force field and (ii) the channel-like acceleration between the counterrotating vortices. In addition, the fluid could be heated up by passing the middle of the gap (small, deep red colored vectors).

IV. DISCUSSION

Although the GeoFlow experiment delivers only interferograms and hence an integrated value of the mean temperature, we are able to deduce some basic properties of the velocity field with accompanying numerical simulations. We find that cold fluid is transported downward underneath channel-like plumes. This is in strong contrast to earlier publications where steep updrafts have been found. Futterer *et al.* [16] explained the specific convective plumes with a massively increased viscosity contrast of $\nu_{\min}/\nu_{\max} = 32$. Although the numerical simulations reproduced well experimentally determined interferograms, the physical process of the viscosity contrast has never been justified. Travnikov *et al.* [26] also analyzed laminar convection in the same numerical and experimental setup for various viscosity contrasts. Very good alignment of sheetlike structures has been found for Ra $< 14\,000$. The turbulent convective case was not in the scope of this study. Zaussinger *et al.* [24] recognized a "stability island" between the conductive and the convective case. The plumes, now known that they are dielectrically produced, have been studied according to their automatized recognition in images. The presented experimental setup is unique for two

reasons. First, the dielectric properties of 1-Nonanol are user friendly. This means that the frequency of the electric field is reasonable low ($f = 10\,650$ Hz) and the loss rates are high ($\tan \delta \approx 0.07$). Second, the given spherical geometry with radius ratio $\eta = 0.5$ delivers a stationary electric field. This favors the numerical solution [15] as the Gauss equation does not have to be solved in each time step. Although the comparison of numerical and experimental interferograms shows many similarities, it reveals one significant issue. We find 38% more plumes in the simulations than in the experiment. Three reasons could explain this discrepancy. First, the numerical simulations have been performed without the cylindrical shaft. Egbers *et al.* [10] examined the influence of the shaft during the construction phase of GeoFlow and estimated a region of influence of $30°$ around the shaft in the southern hemisphere. However, the influence of the shaft might extend over a wider zone in convective flows. Second, the experimental interferograms do not show all plumes, as the visibility depends on the polarization plane. Plumes occur and vanish depending on their position according to the polarization plane. This also reduces the amount of actually counted experimental plumes and implies that we find all plumes in the numerical simulations, but only a fraction of them in the experiment. Third, the plumes observed in the simulation are undergoing merging processes (see [25]) and the number of plumes converges towards the experimental amount.

V. CONCLUSION

The behavior of a liquid layer in the gap between two concentric spherical electrodes has been investigated by means of numerical simulations and the microgravity experiment GeoFlow. The liquid was heated internally by dielectric heating, which leads to thermal convection. The isothermal conductive case was analyzed with a simple 1D temperature equation, which involves a source term arising from the dielectric heating. We found that dielectric heating leads to a parabolic-shaped thermal profile, where the maximum was found in the middle of the gap.

Three-dimensional numerical simulation showed that convection does not set in for $V_0 = 1800$ V, but for $V_0 \geqslant 3000$ V. The onset of convection is expected in between. In addition, we found Nusselt numbers less than unity, which was explained by a negative convective flux in the inner part of the spherical gap. Incorporating the dielectric heating in the equations governing the TEHD convection delivered the best match between numerical and experimental interferograms for GeoFlow II. With increasing voltage, a series of experimental interferograms could be reproduced by numerical simulations.

The GeoFlow experiment does not deliver direct information about the temperature field. Additionally, the velocity field is not accessible, except drift rates of plumes. The temperature distribution is given as an interferogram which represents a radially averaged temperature value and therefore a projection of the full temperature field on the 2D plane. The loss of information is intrinsic owing to the measurement technique. However, the present numerical simulation can complete the experimental measurements. Confronting experimental interferograms with those produced by the simulation, we can deduce basic features of the temperature fields and identify convective plumes and laminar structures in the flow. The simulation also provides associated velocity fields.

Future work could apply the presented TEHD model in situations with an initial temperature contrast. This could explain further inconsistencies in similar experiments. The extension to rotational cases is also in the scope of envisaged work.

ACKNOWLEDGMENTS

construction of the GeoFlow experiment and R. Golinske for discussions about dielectric materials. All simulations were performed at the Northern German Network for High-Performance Computing (HLRN) and the Heraklit cluster (BTU Cottbus-Senftenberg).

[1] J. Staněk, *Electric Melting of Glass* (Elsevier, Amsterdam, 1977).

[2] A. C. Metaxas and R. J. Meredith, *Industrial Microwave Heating* (Peregrinus, London, 1983).

[3] A. R. von Hippel, *Dielectric Materials and Applications* (Artech House, Norwood, 1954).

[4] C. Gabriel, S. Gabriel, E. H. Grant, B. S. J. Halstead, and D. M. P. Mingos, Dielectric parameters relevant to microwave dielectric heating, Chem. Soc. Rev. **27**, 213 (1998).

[5] D. El Khaled, N. Novas, J. A. Gázquez, R. M. García, and F. Manzano-Agugliaro, Alcohols and alcohols mixtures as liquid biofuels: A review of dielectric properties, Renew. Sust. Energy Rev. **66**, 556 (2016).

[6] J. A. Stratten, *Electromagnetic Theory* (McGraw-Hill, New York, 1941).

[7] T. F. Irvine and J. P. Hartnett, *Advances in Heat Transfer* (Elsevier, Amsterdam, 1979).

[8] T. B. Jones, *Electrohydrodynamically Enhanced Heat Transfer in Liquids: A Review* (Elsevier, Amsterdam, 1979).

[9] L. D. Landau and E. M. Lifshitz, *Electrodynamics of Continuous Media* (Elsevier Butterworth-Heinemann, Burlington, 1984).

[10] C. Egbers, W. Beyer, A. Bonhage, R. Hollerbach, and P. Beltrame, The GeoFlow-experiment on ISS (part I): Experimental preparation and design of laboratory testing hardware, Adv. Space Res. **32**, 171 (2003).

[11] K. G. Ayappa, S. Brandon, J. J. Derby, H. T. Davis, and E. A. Davis, Microwave driven convection in a square cavity, AIChE J. **40**, 1268 (1994).

[12] Q. Zhang, T. H. Jackson, and A. Ungan, Numerical modeling of microwave induced natural convection, Int. J. Heat Mass Transfer **43**, 2141 (2000).

[13] P. Ratanadecho, K. Aoki, and M. Akahori, A numerical and experimental investigation of the modeling of microwave heating for liquid layers using a rectangular wave guide (effects of natural convection and dielectric properties), Appl. Math. Model. **26**, 449 (2002).

[14] R. Cherbański and L. Rudniak, Modelling of microwave heating of water in a monomode applicator—Influence of operating conditions, Int. J. Therm. Sci. **74**, 214 (2013).

[15] V. Travnikov, C. Egbers, and R. Hollerbach, The GeoFlow-experiment on ISS (part II): Numerical simulation, Adv. Space Res. **32**, 181 (2003).

[16] B. Futterer, A. Krebs, A.-C. Plesa, F. Zaussinger, R. Hollerbach, D. Breuer, and C. Egbers, Sheet-like and plume-like thermal flow in a spherical convection experiment performed under microgravity, J. Fluid Mech. **735**, 647 (2013).

[17] H. N. Yoshikawa, M. T. Fogaing, O. Crumeyrolle, and I. Mutabazi, Dielectrophoretic Rayleigh-Bénard convection under microgravity conditions, Phys. Rev. E **87**, 043003 (2013).

[18] M. T. Fogaing, H. N. Yoshikawa, O. Crumeyrolle, and I. Mutabazi, Heat transfer in the thermo-electro-hydrodynamic convection under microgravity conditions, Eur. Phys. J. E **37**, 35 (2014).

[19] I. Mutabazi, H. N. Yoshikawa, M. T. Fogaing, V. Travnikov, O. Crumeyrolle, B. Futterer, and C. Egbers, Thermo-electro-hydrodynamic convection under microgravity: A review, Fluid Dyn. Res. **48**, 061413 (2016).

[20] C. Kang, K.-S. Yang, and I. Mutabazi, Thermal effect on large-aspect-ratio Couette-Taylor system: Numerical simulations, J. Fluid Mech. **771**, 57 (2015).

[21] V. Travnikov, O. Crumeyrolle, and I. Mutabazi, Numerical investigation of the heat transfer in cylindrical annulus with a dielectric fluid under microgravity, Phys. Fluids **27**, 054103 (2015).

[22] R. J. Turnbull, Effect of dielectrophoretic forces on the Bénard instability, Phys. Fluids **12**, 1809 (1969).

[23] H. G. Weller, G. Tabor, H. Jasak, and C. Fureby, A tensorial approach to computational continuum mechanics using object-oriented techniques, Comput. Phys. **12**, 620 (1998).

[24] F. Zaussinger, A. Krebs, V. Travnikov, and C. Egbers, Recognition and tracking of convective flow patterns using Wollaston shearing interferometry, Adv. Space Res. **60**, 1327 (2017).

[25] F. Feudel, N. Seehafer, L. S. Tuckerman, and M. Gellert, Multistability in rotating spherical shell convection, Phys. Rev. E **87**, 023021 (2013).

[26] V. Travnikov, F. Zaussinger, P. Beltrame, and C. Egbers, Influence of the temperature-dependent viscosity on convective flow in the radial force field, Phys. Rev. E **96**, 023108 (2017).